ASEAN Journal of Science and Engineering

Journal homepage: http://ejournal.upi.edu/index.php/AJSE/

Analysis of Electric Vehicle (EV) Transmission Performance through Helical Rotor Gear Systems with Variable Helix Angles

Ali Raad Hassan[1], Aws Taha Jadoo[1], Sadeq Hussein Bakhy[1], Emad Kadum Njim[2,], Firas Thair Al-Maliky[3]*

[1] University of Technology, Baghdad, Iraq
[2] State Company for Rubber and Tires Industries, Ministry of Industry and Minerals, Najaf, Iraq
[3] Al-Mustaqbal University, Hillah, Iraq
*Correspondence: E-mail: emad.njim@gmail.com

ABSTRACT

This study investigates the effect of helix angle on the performance of electric vehicle transmission systems using a helical-rotor-geared test apparatus. Several gears and pinions with different helix angles were manufactured and tested at two rotational speeds. The research combined theoretical modeling and finite element analysis to calculate natural frequencies, followed by vibration analysis using an experimental setup. The Fast Fourier Transform was applied to accelerometer data to evaluate the dynamic behavior. The results showed that larger helix angles reduced vibration amplitude and noise levels. This occurs because smoother meshing at higher angles leads to improved load distribution and lower transmission disturbances. The combination of simulation and physical testing supports the optimization of gear dynamics in electric vehicle powertrains, contributing to quieter and more efficient systems.

ARTICLE INFO

Article History:
Submitted/Received 02 Apr 2025
First Revised 24 May 2025
Accepted 13 Jul 2025
First Available online 14 Jul 2025
Publication Date 01 Sep 2025

Keyword:
Dynamic response,
Electrical vehicles,
FEA,
Helical gears,
Helix angle.

1. INTRODUCTION

Electric vehicles (EVs) are increasingly recognized as sustainable and environmentally responsible alternatives to traditional internal combustion engine vehicles. Many reports regarding EVs have been well-documented [1]. They offer significant advantages, including zero tailpipe emissions, higher energy efficiency, and integration potential with renewable energy sources, thereby promoting reduced air pollution and improved public health outcomes [2]. The global shift toward green mobility has intensified research on enhancing EV powertrain components to meet performance, reliability, and energy optimization requirements [3,4]. This also support current issues in sustainable development goals (SDGs) relates to the energy [5-10].

Unlike conventional vehicles, many EVs do not require complex multi-speed gearboxes due to the direct torque output of electric motors. However, the integration of single-speed or multi-speed transmissions can enhance performance, regenerative braking, and driving efficiency [11]. Helical gears, characterized by their angled teeth, have emerged as a valuable alternative to spur and bevel gears due to their ability to transmit power smoothly, quietly, and efficiently [12,13]. Their higher load-carrying capacity and lower noise characteristics make them well-suited for high-performance EV powertrains. Prior research has explored various aspects of gear dynamics, such as gear coatings, tooth modifications, and meshing stiffness [14–18], yet comprehensive studies on the specific role of helix angle in dynamic gear behavior remain limited.

The helix angle plays a critical role in determining gear system behavior by affecting the direction and magnitude of contact forces, meshing smoothness, and vibration characteristics. Correctly designed helix angles can minimize vibration and noise while improving torque transmission and gear lifespan [19–24]. Although some investigations have focused on helical gear modeling or tooth wear progression [20,21], there remains a gap in understanding how varying helix angles influence dynamic responses in operational EV transmission systems. Therefore, this study aims to analyze the effect of helix angle on the vibration behavior of a helical-rotor-geared test apparatus under dynamic conditions. The novelty of this work lies in its combined application of theoretical modeling, finite element simulation, and experimental signal processing, offering a comprehensive and practical insight into optimizing gear design for quieter and more efficient electric vehicle powertrains.

2. METHODS

Figure 1a demonstrates the dimensions of the adopted helical gears in mm, while **Figure 1b** illustrates the test rig development plan. The upper shaft will contain two ball bearings to hold the shaft and a helical gear in the middle, acting like a gear. On the left side, a load will be added. The lower shaft consists of the same ball bearings and a pinion helical gear that transmits motion to the upper shaft. The lower shaft takes its motion and power from a motor through a belt drive. The planned test rig will be more detailed and explained in the upcoming experimental section.

DOI: https://doi.org/10.17509/ajse.v5i2.87802
p- ISSN 2776-6098 e- ISSN 2776-5938

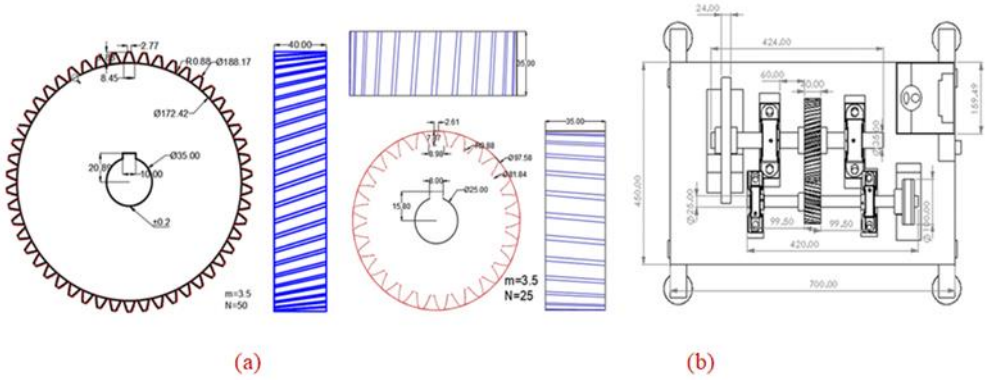

Figure 1. Gear model for the rotational system: (a) Helical gear dimensions; (b) Test rig sketch.

It is noteworthy that the system under consideration involves eight axes to describe its motion. However, to simplify the model and reduce its degrees of freedom to 3, an assumption was made that the gear with its tooth acts as a single rigid entity, and the two axes (shafts) were treated as springs in the direction of rotation, as depicted in **Figure 2**. **Table 1** describes the adopted symbols along with their units. The Steel Structure System was employed to provide a stable speed load, a rigid model, and the gear system's most basic dynamic loading model. The input torque generates a velocity angle to represent the static moment in **Figure 2**, which can be calculated using the moment of inertia formula (equation (1)) [25].

Table 1. Parameters and symbols.

Symbol	Parameter	Unit
IP	Moment of Inertia for Pulley	kg.m^2
IGP	Moment of Inertia for Pinion	kg.m^2
IF	Moment of Inertia for flywheel	kg.m^2
IGG	Moment of Inertia for Gear	kg.m^2
I'G	Equivalent Mass Moment of Inertia for Gears Meshing	kg.m^2
l1	Length of small shaft	M
l2	Length of the big shaft	M
K1	Stiffness of the small shaft	N/m
K2	Stiffness of the big shaft	N/m
K'2	Equivalent stiffness of the big shaft	N/m
ω_n	Natural Frequency	Hz
ω_{mesh}	Rotation Frequency of the Gear Shaft	Hz
nG	The Rotational Speed of the Gear	Rpm
nP	The Rotational Speed of the Pinion	Rpm
N2	Number of Gear Teeth	-
N1	Number of the Pinion Teeth	-
OM	Equation of motion	-

$$I_{read} = I_P + I_{GP} + [(I_{GG} + I_F)(\frac{1}{i})^2] \quad (1)$$

Then the angular accelerations are in equation (2):

$$\ddot{\theta}_1 = \ddot{\theta}_2 = \frac{M_T}{I_{read}}, \ddot{\theta}_4 = \ddot{\theta}_3 = \ddot{\theta}_1(\frac{1}{i}) \quad (2)$$

DOI: https://doi.org/10.17509/ajse.v5i2.87802
p- ISSN 2775-6793 e- ISSN 2775-6815

The two gearbox shafts have different torque values, measured using the free-body diagram (equations (3) and (4)):

$$M_1 = (I_{read} - I_p)\ddot{\theta}_1 \tag{3}$$

$$M_4 = \ddot{\theta}_4 I_4 \tag{4}$$

When applying the assumptions in the equations to simplify the system to find its natural frequency, through these assumptions, it turns from 8DOF to 3DOF. **Figure 2b** shows the lowering oscillator chain of the drive gear system with an arbitrary standard model compared to **Figure 2a**.

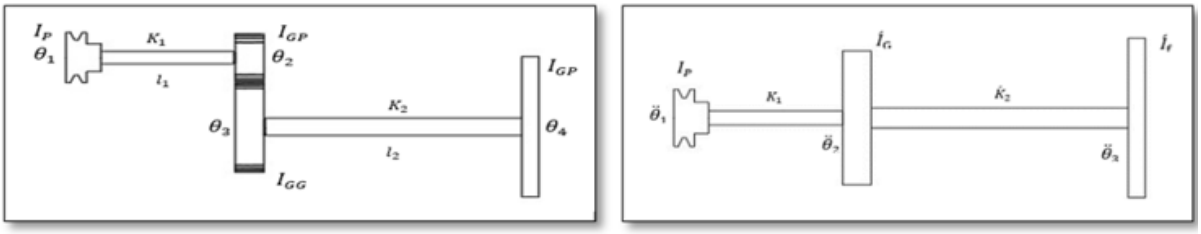

(a) (b)

Figure 2. Gear model for the rotational system: (a) Full model; (b) Equivalent model.

To further continue the equations of motion to calculate the natural frequencies (equations (5), (6), and (7)):

$$I_P\ddot{\theta}_1 + K_1\theta_1 - K_1\theta_2 = 0 \tag{5}$$

$$I'_G\ddot{\theta}_2 - K_1\theta_1 + (K_1 + K'_2)\theta_2 - K'_2\theta_3 = 0 \tag{6}$$

$$I'_f\ddot{\theta}_3 - K'_2\theta_2 + K'_2\theta_3 = 0 \tag{7}$$

The matrix will be in equation (8):

$$\begin{bmatrix} I_P & 0 & 0 \\ 0 & I'_G & 0 \\ 0 & 0 & I'_F \end{bmatrix}\begin{bmatrix} \ddot{\theta}_1 \\ \ddot{\theta}_2 \\ \ddot{\theta}_3 \end{bmatrix} + \begin{bmatrix} K_1 & -K_1 & 0 \\ -K_1 & (K_1 + K'_2) & -K'_2 \\ 0 & -K'_2 & K'_2 \end{bmatrix}\begin{bmatrix} \theta_1 \\ \theta_2 \\ \theta_3 \end{bmatrix} = 0 \tag{8}$$

To find the natural frequency is by solve (EOM; the natural frequency is determined from this equation (9):

$$-\omega_n{}^2\left[\omega_n{}^4 - \omega_n{}^2\left(K_1\frac{I_P + I'_G}{I_P I'_G} + K'_2\frac{I'_G + I'_F}{I'_G I'_F}\right) + K_1K'_2\frac{I_P + I'_G + I'_F}{I_P I'_G I'_F}\right] = 0 \tag{9}$$

To find the natural frequencies, we used equation (10):

$$\omega_n{}^2{}_{2,3} = \frac{1}{2}\left(K_1\frac{I_P + I'_G}{I_P I'_G} + K'_2\frac{I'_G + I'_F}{I'_G I'_F}\right) \mp \sqrt{\frac{1}{4}\left(K_1\frac{I_P + I'_G}{I_P I'_G} + K'_2\frac{I'_G + I'_F}{I'_G I'_F}\right) - K_1K'_2\frac{I_P + I'_G + I'_F}{I_P I'_G I'_F}} \tag{10}$$

In this section, the results of the vibration response are presented, where the natural frequencies of both the theoretical basis and the finite element analysis are compared and described accordingly.

DOI: https://doi.org/10.17509/ajse.v5i2.87802
p- ISSN 2776-6098 e- ISSN 2776-5938

2.2. Finite Element Analysis

Finite element analysis is used in modern technologies to validate the results obtained by theoretical investigation [26-29]. In this study, a test rig was built using a computer-aided design by Pappalardo et al. [29], where the SolidWorks program was utilized to save the file as a Parasolid for later use in finite element analysis. Computer-aided engineering (CAE) relies primarily on computer-aided design (CAD) software, commonly called CAE tools, which are utilized for robustness and performance assessments. These tools enable simulation, validation, and optimization of manufacturing equipment and products. CAE applies to diverse industries, including automotive, aviation, space, and shipbuilding. According to [30], ANSYS software was utilized for modal simulation, employing the 2020 ANSYS engineering data sources, and the materials generated for the sections of the open gear system test rig were integrated into the simulation workbench. The SolidWorks rotary gear system was constructed by generating and importing the geometry using the Parasolid extension. Six mode shapes were selected for comparison, considering that higher mode shape orders result in increased natural frequencies, leading to wider deviations from the operational Frequency ranges. **Figure 3** visually presents the six mode shapes of the system. We showed several modes: Mode shape 1 (**Figure 3(a)**); Mode shape 2 (**Figure 3(b)**); Mode shape 3 (**Figure 3(c)**); Mode shape 4 (**Figure 3(d)**); Mode shape 5 (**Figure 3(e)**); Mode shape 6 (**Figure 3(f)**).

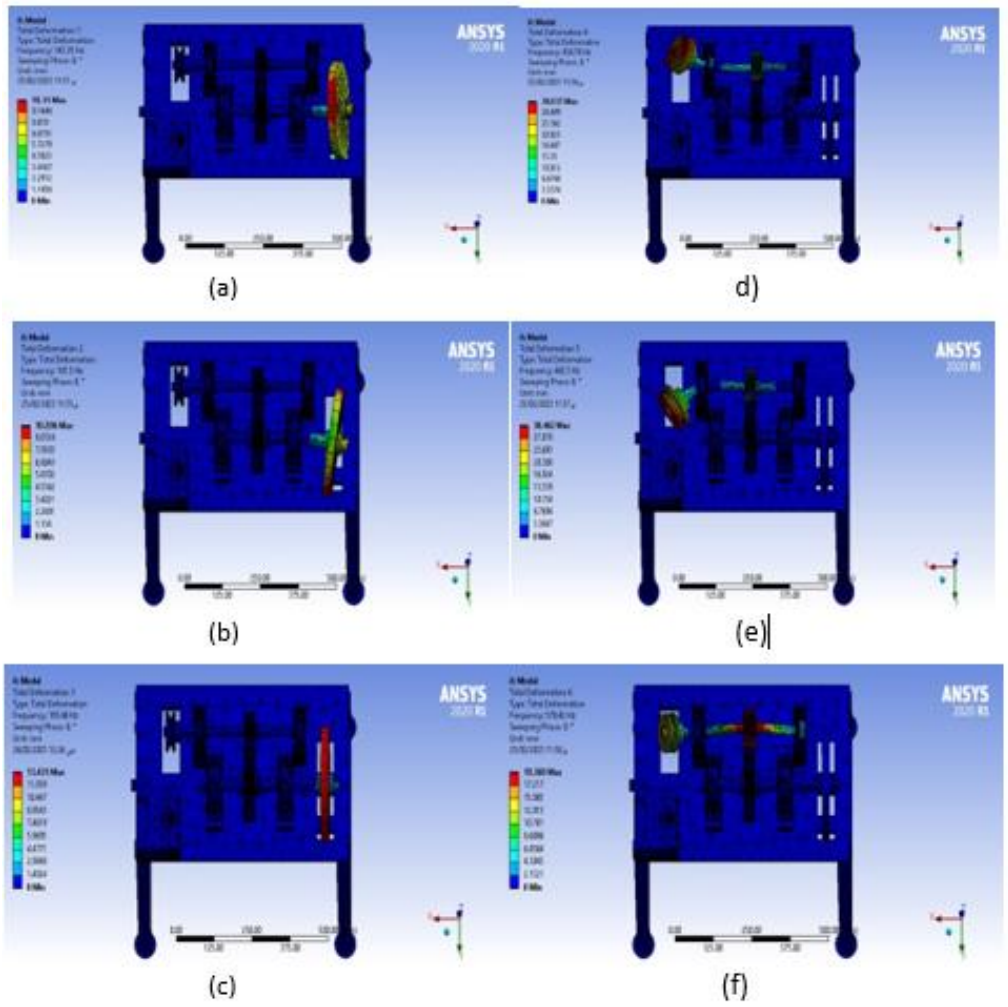

Figure 3. FEA natural frequencies: (a) Mode shape 1; (b) Mode shape 2; (c) Mode shape 3; (d) Mode shape 4; (e) Mode shape 5; (f) Mode shape 6.

DOI: https://doi.org/10.17509/ajse.v5i2.87802
p- ISSN 2775-6793 e- ISSN 2775-6815

The deformation in mm of the six mode shapes was presented. The first three mode shapes are presented as failures in the load, specifically the flywheel. Subsequently, the other three mode shapes are presented as failures in the gear where the belt drive is fixed and the input rotational speed starts.

3. EXPERIMENTAL APPROACH

3.1 Methodology

The approach used to gather the gear system readings involves using a vibration accelerometer [31,32] accompanied by a DAQ-6009 data acquisition device. The gathered time-domain vibration signals are processed by a LabVIEW software block diagram that employs an FFT to transform them into frequency-domain vibration signals. The specifications for the ADXL335 vibration accelerometer can be found in **Table 2**.

Table 2. Natural frequencies results.

No.	Specifications	Information
1	Dimension	21 x 16 x 10 mm
2	Sensitivity	300 mV/g
3	Bandwidth	0.5-1600 Hz (X, Y axes) and 0.5-550 Hz (Z axes)

3.2 Test Rig Design and Development

The ADXL335 accelerometers are strategically mounted atop the bearings, with the Y-axis oriented along the rotating shaft line, the X-axis aligned with the operating floor, and the Z-axis positioned orthogonal to the operating table. The experimental setup comprises two shafts, as illustrated in **Figure 4**. The first shaft encompasses a flywheel and two supporting bearings, with a helical gear between them. The second shaft comprises a pinion and two additional bearings, with a pulley attached to the right-side bearing's extension. An electric motor drives the pulley through a belt drive, whose input rotational operating speed is regulated by an AC driver. The tachometer is employed to determine the operational speed of both shafts, utilizing a white tape affixed to the pulley and flywheel. The ADXL335 is interfaced with a data acquisition device, the DAQ-6009, to obtain voltage input data, which is subsequently processed using the PC platform software LabVIEW to compute acceleration data [31,32]. The obtained vibrational time-domain signals are then converted to frequency-domain signals utilizing FFT, and the resulting measurements are saved as a file on the PC platform. This process is repeated four times due to the variable helix angle associated with the gears and pinions.

3.3 Signal Processing utilizing LabVIEW

A DAQ assistant add-in is employed to control the DAQ-6009 device and capture voltage input data, with a sensitivity of 0.3 used to generate acceleration signals. Each sensor has three axes, so the signal is divided into six outputs. The arithmetic mean equation 6 consistently calibrates signals, where m represents the number of input signals. An example block diagram created with the LabVIEW software is illustrated in **Figure 5**. Spectral measurements analyze the frequency domain for each of the three signals. The sampling frequency is set at 500 Hz, as no operational speed will exceed this value by more than half. The number of samples is set to 1000 to increase the output resolution, and the program is executed 1000 times in a loop. **Table 3** presents the four primary helix angles examined at two rotational speeds of 1500 and 2000 rpm.

DOI: https://doi.org/10.17509/ajse.v5i2.87802
p- ISSN 2776-6098 e- ISSN 2776-5938

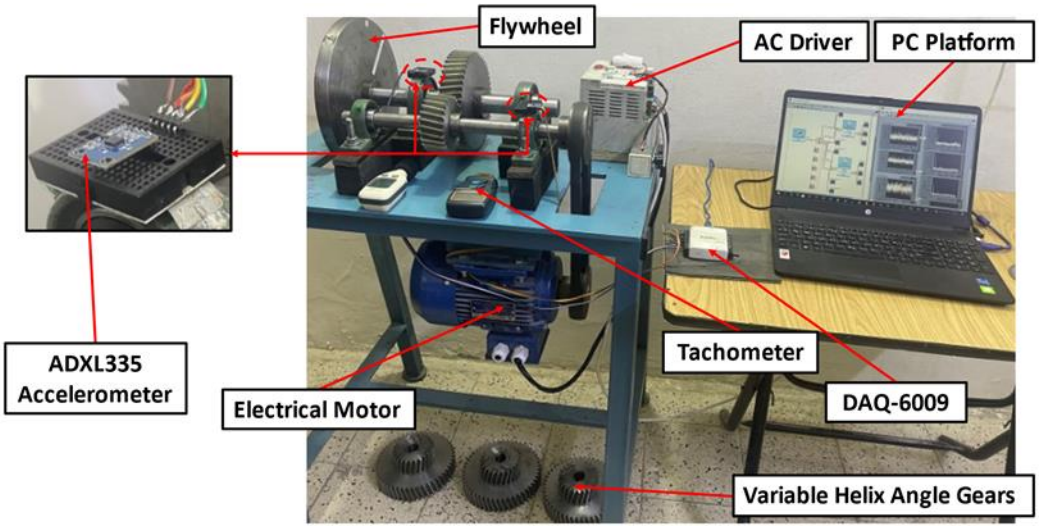

Figure 4. Experimental Setup.

$$\text{Arithmetic Mean} = \frac{1}{m}\sum_{i=1}^{m} X_i \quad (11)$$

Table 3. Studied cases.

Studied Case No.	1	2	3	4
Helix Angle (Degrees)	9	11	13	15

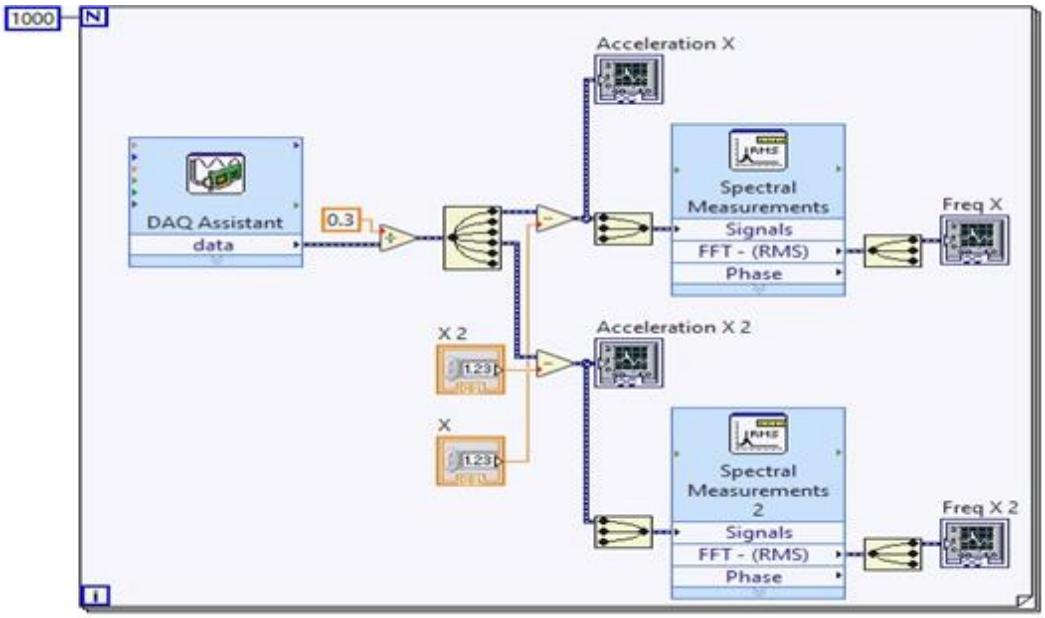

Figure 5. Sample of the total work signal processing block diagram.

4. RESULTS AND DISCUSSION

4.1 Natural frequencies of Theoretical Basis and FEA

Table 4 presents the natural frequencies derived from Finite Element Analysis (FEA) and a theoretical foundation. The utilization of Finite Element Analysis (FEA) is conducive to introducing all six natural frequencies. Conversely, the theoretical equations of the reduced system with three degrees of freedom will only introduce three natural frequencies. Theoretically, the initial natural Frequency derived from equation 9 is consistently zero due

DOI: https://doi.org/10.17509/ajse.v5i2.87802
p- ISSN 2775-6793 e- ISSN 2775-6815

to its restricted computational capacity. The value of the second natural Frequency is 195.667 Hz. The value of 534.896 Hz represents the third natural Frequency as determined through theoretical means. After applying finite element analysis on the test rig, it was observed that the first natural Frequency is 143.35 Hz, as opposed to zero. The second natural Frequency is observed to be novel, with a numerical value of 181.5 Hz. The third natural Frequency, ascertained through Finite Element Analysis (FEA), exhibits a level of similarity with the second natural Frequency derived from a theoretical approach.

Additionally, correspondingly, the third and fourth inherent frequencies exhibit magnitudes of 436.78 and 482.3 Hz. The sixth and ultimate natural Frequency derived from the analysis exhibits a marginally greater value of 578.42 Hz compared to the third and ultimate natural Frequency obtained through the theoretical framework. Utilizing finite element analysis can address the inadequacy of calculations about the three degrees of freedom equation. This leads to a broader spectrum of possible natural frequencies, thereby providing a more comprehensive understanding of the operating system frequencies that can be effectively avoided to prevent faults.

Table 4. Natural frequencies results.

Natural Frequency Order (Mode Shape)	Finite Element Analysis Results	Theoretical Results
1	143.35	0
2	181.5	195.667
3	193.46	534.896
4	436.78	-
5	482.3	-
6	578.42	-

4.1 Experimental Results

Figure 6 illustrates the frequency response during operation utilizing FFT analysis. The gear-pinion pairs were tested at two distinct operational speeds, and four-helix angles were employed. The horizontal axis, or X-axis, denotes the range of frequencies in Hertz. In contrast, the vertical axis, or Y-axis, indicates the amplitude or occurrence of the Frequency in a dimensionless manner. We used several degrees of helix angles: 9-degree helix angle (**Figure 6(a)**); 11-degree helix angle (**Figure 6(b)**); 13-degree helix angle (**Figure 6(c)**); and 15-degree helix angle (**Figure 6(d)**).

The results indicate that the dynamic response at an operating speed of 1500 RPM exhibits a higher amplitude regardless of its placement. In contrast, the amplitude value is lower at an operating speed of 2000 RPM. Moreover, an inverse relationship is observed between the peak values of Frequency amplitudes and the operating helix angle, such that higher operating helix angles result in lower peak values. At an operational speed of 2000 RPM, it has been observed that there are three peak values present at helix angles of 9 and 11 degrees. However, when the helix angle is increased to 13 and 15 degrees, the number of peaks decreases to one. A decrease in peak values corresponds to a reduction in dynamic response, attributed to smoother speed transmission mechanisms. The phenomenon described can be discerned at the operational velocity of 1500 RPM, wherein the magnitudes and maximum values exhibit a reduction with an increase in the operational helix angle.

It is crucial to note that the peaks above correspond to the frequencies of the bearings in operation, the meshing Frequency, and the motor Frequency values. Including the peak value location description is deemed superfluous, given that the primary objective of this

DOI: https://doi.org/10.17509/ajse.v5i2.87802
p- ISSN 2776-6098 e- ISSN 2776-5938

investigation is to illustrate the influence of the aforementioned helix angles on transmission performance, wherein comparable operating conditions result in reduced amplitudes.

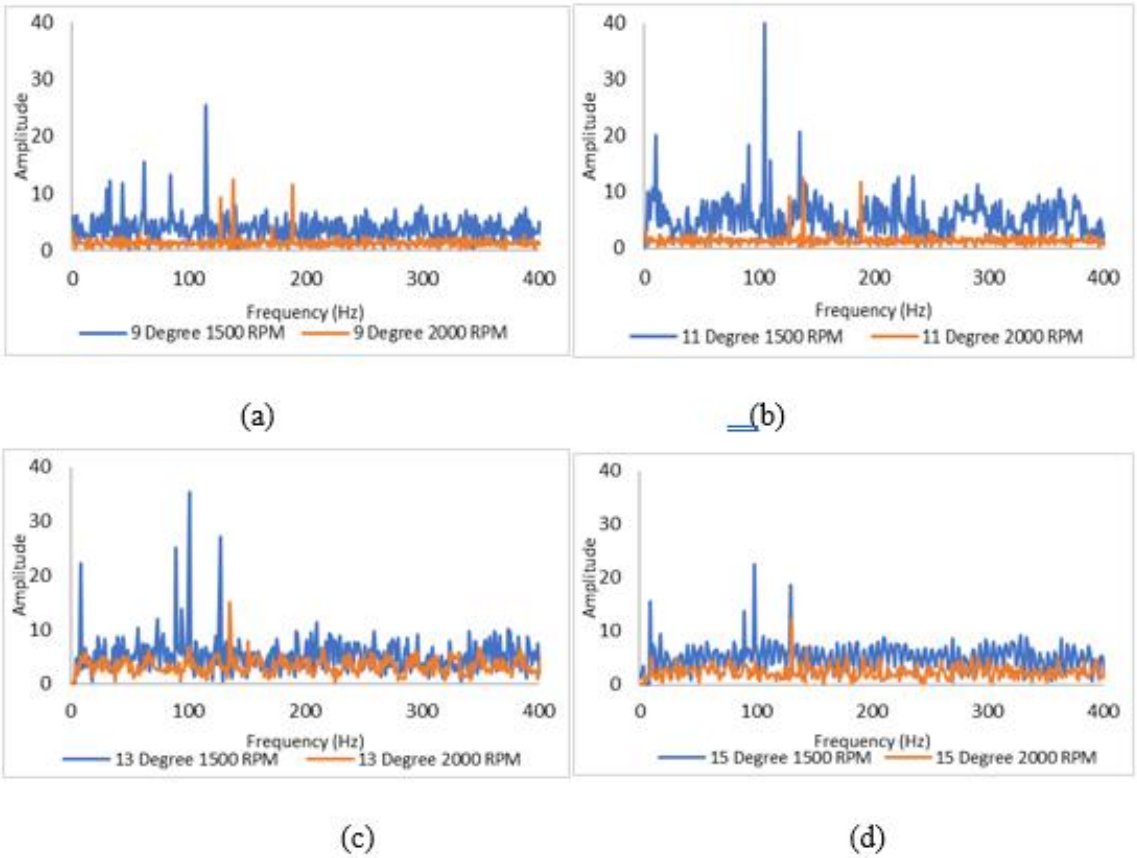

Figure 6. Frequency response at 1500 and 2000 RPM operating speeds: (a) 9-degree helix angle; (b) 11-degree helix angle; (c) 13-degree helix angle; and (d) 15-degree helix angle.

5. CONCLUSION

This study analyzes a rotor-geared test apparatus for helical gears, considering the adaptability of gear foundations and rotary dynamics. Finite Element Analysis is employed to ascertain and compare the inherent frequencies with the theoretically computed values. The study involved the production of several helical pinions and gears, each with four distinct helix angles and a consistent number of teeth. This experiment aimed to investigate the impact of the helix angle on the resulting products' vibration response and noise reaction. The experimental dynamic Frequency was determined through signal processing utilizing the Fast Fourier Transform under two distinct rotational operating speeds. The ensuing frequencies were subjected to analysis, revealing that a reduced helix angle leads to heightened out-of-plane vibration and commotion in the gear structure. The findings indicate that the helix angle significantly impacts the dynamic system's overall functioning, thereby affecting the potential research on gear systems for electric vehicles.

6. ACKNOWLEDGMENT

The authors wish to thank the Ministry of Higher Education and Scientific Research, University of Technology /Iraq, for using facilities in their labs.

DOI: https://doi.org/10.17509/ajse.v5i2.87802
p- ISSN 2775-6793 e- ISSN 2775-6815

7. AUTHORS' NOTE

The authors declare that there is no conflict of interest regarding the publication of this article. Authors confirmed that the paper was free of plagiarism.

8. REFERENCES

[1] Aziz, M., Huda, M., Nandiyanto, A.B.D., and Abdullah, A.G. (2018). Opportunity of frequency regulation using electric vehicles in Denmark. *Journal of Engineering, Science and Technology*, 13(6), 1700-1712.

[2] Saldarriaga-Zuluaga, S. D., López-Lezama, J. M., Zuluaga Ríos, C. D., & Villa Jaramillo, A. (2022). Effects of the incorporation of electric vehicles on protection coordination in microgrids. *World Electric Vehicle Journal*, 13(9), 163.

[3] Ning, X., Chen, M., Zhou, Z., Shu, Y., Xiong, W., Cao, Y., Shang, X., and Wang, Z. (2022). Thermal analysis of automobile drive axles by the thermal network method. *World Electric Vehicle Journal*, *13*(5), 75.

[4] Arango, I., and Escobar, D. (2022). Integration of a chassis servo-dynamometer and simulation to increase energy consumption accuracy in vehicles emulating road routes. *World Electric Vehicle Journal*, *13*(9), 164.

[5] Soegoto, H., Soegoto, E.S., Luckyardi, S., and Rafdhi, A.A. (2022). A bibliometric analysis of management bioenergy research using vosviewer application. *Indonesian Journal of Science and Technology*, *7*(1), 89-104.

[6] Jelita, R., Nata, I.F., Irawan, C., Jefriadi, J., Anisa, M.N., Mahdi, M.J., and Putra, M.D. (2023). Potential alternative energy of hybrid coal from co-pyrolysis of lignite with palm empty fruit bunch and the kinetic study. *Indonesian Journal of Science and Technology*, *8*(1), 97-112.

[7] Jamilatun, S., Aziz, M., and Pitoyo, J. (2023). Multi-distributed activation energy model for pyrolysis of sugarcane bagasse: Modelling strategy and thermodynamic characterization. *Indonesian Journal of Science and Technology*, *8*(3), 413-428.

[8] Hamidah, I., Ramdhani, R., Wiyono, A., Mulyanti, B., Pawinanto, E.E., Hasanah, L., Diantoro, M., Yuliarto, B., Yunas, J., and Rusydi, A. (2023). Biomass-based supercapacitors electrodes for electrical energy storage systems activated using chemical activation method: A literature review and bibliometric analysis. *Indonesian Journal of Science and Technology*, *8*(3), 439-468.

[9] Wangsupphaphol, A., Phichaisawat, S., and Lengkayan, R. (2024). Alternative energy options for a Thai durian farm: Feasibility study and experiments for the combination of solar photovoltaics and repurposed lithium-ion batteries. *Indonesian Journal of Science and Technology*, *9*(1), 125-144.

[10] Krishnan, A., Al-Obaidi, A.S.M., and Hao, L.C. (2024). Towards sustainable wind energy: A systematic review of airfoil and blade technologies over the past 25 years for supporting sustainable development goals (SDGs). *Indonesian Journal of Science and Technology, 9*(3), 623-656.

[11] Du, J., Hu, L., Mao, J., and Zhang, Y. (2021). optimal vibration suppression modification method for high-speed helical gear transmission of battery electric vehicles under full working conditions. *Machines*, *9*(10), 226.

[12] Ahmed, A., and Ali Raad Hassan (2023). Experimental and numerical study of spur gears with lightning holes. *Engineering and Technology Journal*, *41*(7), 1-11.

DOI: https://doi.org/10.17509/ajse.v5i2.87802
p- ISSN 2776-6098 e- ISSN 2776-5938

[13] Ali Raad Hassan (2022). Effects of rotational speed on the natural frequency of the differential bevel gear. *Eastern-European Journal of Enterprise Technologies*, *4*(1) (118), 56–63.

[14] Jäger, S., Schätzle, J., and Linde, T. (2022). Top-down validation framework for efficient and low noise electric-driven vehicles with multi-speed gearbox. *World Electric Vehicle Journal*, *13*(12), 228.

[15] Lee, C. H., Kang, Y. K., Kim, D. K., Kim, S. H., and Moon, Y. H. (2023). Process design for manufacturing fiber-reinforced plastic helical gears using a rapid heating and cooling system. *Metals*, *13*(3), 483.

[16] Cheng, X., Li, Z., Cao, C., Wang, Y., Ding, N., and Wu, G. (2022). Dynamic analysis and fault diagnosis for gear transmission of a vibration exciter of a mine-used vibrating screen under different conditions. *Applied Sciences*, *12*(24), 12970.

[17] Ayuketang Arreyndip, N., Moise Dikande, A., and Joseph, E. (2018). Nonlinear multi-frequency dynamics of wind turbine components with a single-mesh helical gear train. *Mathematical and Computational Applications*, *23*(1), 12.

[18] Chen, Y.-C. (2020). Time-varying dynamic analysis of a helical-geared rotor-bearing system with three-dimensional motion due to shaft deformation. *Applied Sciences*, *10*(4), 1542.

[19] Yang, Y., Wu, Y., Li, Y., and Liu, X. (2023). Effects of tooth modification in the involute helical gear form-grinding process on loaded transmission character with consideration of tooth axial inclination error. *Machines*, *11*(2), 305.

[20] Sun, X., Wang, T., Zhang, R., Gu, F., and Ball, A. D. (2021). Numerical modelling of vibration responses of helical gears under progressive tooth wear for condition monitoring. *Mathematics*, *9*(3), 213.

[21] Li, G., Chen, Y., Zang, L., Liu, R., Ju, D., Wu, Y., and Tan, Y. (2021). Comparative study on transmission performance of manganese phosphate coated gears. *Coatings*, 11(9), 1026.

[22] Li, Y., Yuan, S., Wu, W., Liu, K., Lian, C., and Song, X. (2022). Vibration analysis of two-stage helical gear transmission with cracked fault based on an improved mesh stiffness model. *Machines*, *10*(11), 1052.

[23] Hou, S., Wei, J., Zhang, A., Zhang, C., Yan, J., and Wang, C. (2020). A novel comprehensive method for modeling and analysis of mesh stiffness of helical gear. *Applied Sciences*, *10*(19), 6695.

[24] Hassan, A. R., Hawas, M. N., Abdullah, A. R., Majdi, H. S., and Habeeb, L. J. (2023). High-speed helical gear design parameters effect on the dynamic stress. *Mathematical Modelling of Engineering Problems*, *10*(4), 1189–1198.

[25] ODA, S., MlYACHIKA, K., and SAYAMA, T. (1986). Effects of rim and web thicknesses on bending fatigue strength of internal gear. *Bulletin of JSME*, 29(248), 586–592.

[26] Al-Haddad, L. A., and Jaber, A. A. (2023). An intelligent fault diagnosis approach for multirotor UAVs based on deep neural network of multi-resolution transform features. *Drones*, *7*(2), 82.

[27] Metteb, Z., Ogaili, A., Mohammed, K., Alsayah, A., Hamzah, M., Al-Sharify, Z., Jaber, A., and Njim, E. (2025). Optimization of hybrid core designs in 3D-Printed PLA+ sandwich structures: An experimental, statistical, and computational investigation completed with bibliometric analysis. *Indonesian Journal of Science and Technology*, *10*(2), 207-236.

[28] Kadum Njim, E., AlMaamori, M. H., MADAN, R., H. Bakhy, S., AlWaily, M., Khobragade, P., and Hadji, L. (2024). Numerical and analytical investigation of free vibration behavior

DOI: https://doi.org/10.17509/ajse.v5i2.87802
p- ISSN 2775-6793 e- ISSN 2775-6815

of porous functionally graded sandwich plates. *Mechanics of Advanced Composite Structures*, *12*(2025), 555–568.

[29] Pappalardo, C. M., Del Giudice, M., Oliva, E. B., Stieven, L., and Naddeo, A. (2023). Computer-aided design, multibody dynamic modeling, and motion control analysis of a quadcopter system for delivery applications. *Machines*, *11*(4), 464.

[30] Al-Haddad, L. A., and Jaber, A. A. (2023). Influence of operationally consumed propellers on multirotor UAVs airworthiness: Finite element and experimental approach. *IEEE Sensors Journal*, *23*(11), 11738–11745.

[31] Ghazali, M. H. M., and Rahiman, W. (2022). An investigation of the reliability of different types of sensors in the real-time vibration-based anomaly inspection in drone. *Sensors*, *22*(16), 6015.

[32] Mouthanna, A., Bakhy, S. H., Al-Waily, M., and Njim, E. K. (2023). Free vibration investigation of single-phase porous fg sandwich cylindrical shells: Analytical, numerical and experimental study. *Iranian Journal of Science and Technology, Transactions of Mechanical Engineering*, 48(3), 1135–1159.

DOI: https://doi.org/10.17509/ajse.v5i2.87802
p- ISSN 2776-6098 e- ISSN 2776-5938